Finding Critical Points and Reconstruction of Electron Densities on Grids

Alberto Otero-de-la-Roza[a)]
Departamento de Química Física y Analítica and MALTA Consolider Team, Facultad de Química, Universidad de Oviedo, 33006 Oviedo, Spain

(Dated: 23 May 2022)

The quantum theory of atoms in molecules (QTAIM), developed by Bader and coworkers, is one of the most popular ways of extracting chemical insight from the results of quantum mechanical calculations. One of the basic tasks in QTAIM is to locate the critical points of the electron density and calculate various quantities (density, Laplacian,...) on them, since these have been found to correlate with molecular properties of interest. If the electron density is given analytically, this process is relatively straightforward. However, locating the critical points is more challenging if the density is known only on a three-dimensional uniform grid. A density grid is common in periodic solids because it is the natural expression for the electron density in plane-wave calculations. In this article, we explore the reconstruction of the electron density from a grid and its use in critical point location. The proposed reconstruction method employs polyharmonic spline interpolation combined with a smoothing function based on the promolecular density. The critical point search based on this reconstruction is accurate, trivially parallelizable, works for periodic and non-periodic systems, does not present directional lattice bias when the grid is non-orthogonal, and locates all critical points of the underlying electron density in all tests studied. The proposed method also provides an accurate reconstruction of the electron density over the space spanned by the grid, which may be useful in other contexts besides critical point localization.

I. INTRODUCTION

The quantum theory of atoms in molecules[1–5] (QTAIM) is a popular and physically grounded way of extracting chemical information from a theoretical or experimental electron density. QTAIM is based on the partition of a molecule or solid into atomic regions known as basins. These atomic basins are bounded by interatomic surfaces defined by a zero-flux condition of the electron density:

$$\nabla\rho(\boldsymbol{x})\cdot\boldsymbol{n}(\boldsymbol{x}) = 0 \tag{1}$$

which holds for all points on the surface, where $\boldsymbol{n}$ is a vector normal to the surface. More simply, gradient paths of the electron density must not cross the atomic basin boundaries. This zero-flux condition ensures that the kinetic energy operator is uniquely defined within the atomic basin, and therefore that the atom can be regarded as a proper open quantum subsystem.[3] By integration over the atomic basins, one can calculate atomic properties such as atomic volumes, electron populations, and many others. An enormous amount of work has been devoted to apply and extend QTAIM since its conception, a work that continues to this day. Because the atomic basins are completely determined by the electron density, QTAIM has also been used extensively for chemical bonding analysis using experimental electron densities.[6–8]

An important aspect of QTAIM is the chemical interpretation of various quantum mechanical properties at the critical points (CP) of the electron density, given by:

$$\nabla\rho(\boldsymbol{x}) = \boldsymbol{0} \tag{2}$$

where $\boldsymbol{0}$ is the zero vector. Except for maxima and the rare cases where degeneracies exist, all critical points of the density lie on an interatomic surface. In particular, the first-order saddle points, known as bond critical points (BCP) in QTAIM, have been used extensively to characterize intra- and intermolecular properties.[1] For instance, the electron density at the BCPs has been shown to correlate with interaction strengths of hydrogen bonds,[6,9–11] as well as other types of non-covalent bonding interactions.[12,13] Recently, BCPs have been used to benchmark various density functional approximations regarding the quality of the ground-state electron densities they produce.[14] Two unique gradient paths of the electron density starting at a BCP connect this critical point with the adjacent nuclei, forming what is known as a bond path in QTAIM. The existence of a bond path is the criterion for the definition of a bond within QTAIM which usually, but not always, coincides with traditional chemical bonds.[15–17] The critical points of scalar fields other than the electron density, such as the Laplacian,[18,19] the electron localization function[20,21] (ELF), or the molecular electrostatic potential[22–25] (MESP) can also be used to extract chemical insight.[26,27]

If the electron density is smooth (there are no artifacts or discontinuities) and its first and second derivatives are known analytically, locating all its critical points is relatively straightforward. For scalar fields more complex than the electron density, more sophisticated approaches may be required.[19,25,28–31] However, it is often the case that electron densities are given numerically as values on a uniform grid and no analytical expression is available. This is the case for periodic densities calculated using a plane-wave basis set, although electron density grids can also be encountered in experimental studies.[32]

[a)] Electronic mail: aoterodelaroza@gmail.com

In practice, an electron density grid is also the only option when the analytical calculation of the density and its derivatives has not been implemented in the program that performs the critical point search, as most electronic structure packages have the ability to calculate and write the density on a grid. Therefore, although locating critical points using the analytical derivatives of the scalar field is the preferred method if possible, it is interesting to devise alternatives for when the analytical derivatives are not available.

The use of electron density grids for QTAIM analysis in periodic solids has experienced a surge in popularity over the past decades thanks to the development of grid-based atomic basin integration algorithms pioneered by Kohout's implementation in the DGrid program,[33–38] which allow the inexpensive calculation of all atomic charges and volumes in the system. Methods for the reliable and automatic location of all critical points from an electron density grid have been proposed in the literature[32,39] and are still a topic of active research.[40] The most natural approach is to extend the electron density by three-dimensional interpolation using the values at the grid nodes. This method has been used in the past,[32,33,39,41–44] and the exploration of its strengths and weaknesses is the subject of this work. The electron density interpolant itself is also useful because it provides a reconstruction of the electron density of the system at points other than the grid nodes, which can also be used for purposes other than locating CPs, such as plotting or other chemical bonding analysis techniques. Therefore, it is important to have a way of accurately performing this reconstruction.

The difficulties with interpolation methods when used for CP location have been highlighted before,.[39,40] In a recent article,[40] a CP search method (TopoMS) was proposed based on Forman's discrete Morse theory,[45] and previous extensive work by some of the authors in the area of computer visualization.[46–50] The TopoMS method works by building a discrete analogue of the density gradient vector field and then classifying the discrete grid elements (vertices, edges, etc.) as critical or non-critical. The set of CPs determined by TopoMS is consistent by construction, which means that the number and type of critical points respects the appropriate sum rules (Eqs. 3 and 4). However, consistency does not imply correctness and, while promising, it has not been shown that the position and properties of the critical points determined by TopoMS agree with those of the underlying (non-discrete) electron density, nor that it is able to find the same full topology as the underlying electron density. Furthermore, it is unclear from the description in the article[40] how the persistence-based cancellation of connected critical points is applied and whether the method allows for an automatic (i.e. without user intervention) and reliable way of finding all critical points from a smooth electron density grid. Lastly, even though the theory as presented by Gyulassy et al.[46–50] is completely general, the actual TopoMS implementation[51] seems to be affected by lattice bias, which is a problem for grids in non-orthogonal periodic solids. This is a recurring problem for grid-based algorithms, which is discussed in the next section.

In this article, we explore the use of interpolation methods to reconstruct the full electron density from values given on a grid, and their use to find the critical points in the system. All methods presented in this work were implemented in the critic2[43,44] program. In particular, it is shown that an interpolant based on polyharmonic splines in combination with a smoothing transformation using the promolecular density is able to reconstruct the electron density in the three-dimensional space spanned by the grid with excellent accuracy. This reconstruction, which is valuable on its own for other purposes, is accurate enough that a simple CP search based on the repeated use of Newton's method is able to find all critical points automatically in all test cases. In addition, the quality of the reconstruction increases with finer grids. However, the interpolation may suffers if artifacts are present in the grid, for instance, aliasing errors from a plane-wave calculation. The proposed interpolation and CP search method locates all critical points within minutes, is trivially parallelizable, works for non-periodic and periodic, orthogonal and non-orthogonal grids and shows no lattice bias by construction.

II. FINDING CRITICAL POINTS OF ELECTRON DENSITY GRIDS

Critical points of the electron density are characterized by the number of non-zero and the number of positive minus negative elements of the Hessian matrix diagonal, respectively known as the rank (r) and signature (s). Assuming no degeneracies exist ($r = 3$), there are three types of critical points: maxima ($s = -3$), first-order saddle points (-1), second-order saddle points (1), and minima (3). In QTAIM, these are commonly referred to as nuclei, bonds, rings, and cages. The term "nuclei" for the maxima is a misnomer because non-nuclear maxima exist,[52–54] but it will be used for simplicity. Each nucleus generates an atomic basin, and all the other critical points (bonds, rings, and cages) are located on the boundaries between those basins. The number and types of critical points in a periodic system (commonly, a solid) have to respect the following constraints:

$$n - b + r - c = 0 \quad ; \quad n, c \geq 1 \quad ; \quad b, r \geq 3 \tag{3}$$

whereas in non-periodic systems (gas-phase molecules):

$$n - b + r - c = 1 \tag{4}$$

where n, b, r, and c are the number of nuclei, bonds, rings, and cages, respectively. These conditions are typically referred to as the Morse (Eq. 3) and Poincaré-Hopf (Eq. 4) sum rules. Each bond connects two maxima via unique ascending gradient paths, known as the bond paths. The set of all bond paths in the system is the molecular graph, and the set of all critical points is its (critical point) topology.

Locating the critical points of an analytical electron density is relatively easy. For this task, a set of points ("seeds") in the system are chosen and Newton's method is started on each seed to try to find a critical point in the vicinity.[28,42–44] In Newton's method, a point sequence is calculated such that:

$$\boldsymbol{x}_{n+1} = \boldsymbol{x}_n - \boldsymbol{H}_\rho^{-1}(\boldsymbol{x}_n)\boldsymbol{\nabla}\rho(\boldsymbol{x}_n) \tag{5}$$

where $\boldsymbol{\nabla}\rho$ is the gradient and $\boldsymbol{H}_\rho$ is the Hessian of the electron density. This sequence may converge to a critical point of any kind (not necessarily a minimum), and the convergence is quadratic when close to the critical point, although convergence is not guaranteed. Past experience with the critic2 program[43,44] has shown that placing 5 seeds between every pair of atoms at most 15 bohr apart (in molecules) or at single-level subdivisions of the irreducible Wigner-Seitz cell[43,44] (in solids) is enough to locate the complete set of critical points in most systems. This seeding strategy is used in all calculations in this work; the number of seeds can be increased or the seeding strategy can be altered for particularly difficult or unusual systems. A point is considered critical when the norm of the electron density gradient falls below a user-controlled threshold. The threshold used throughout this work (and the default in critic2) is 1×10^{-12} atomic units.

Let us assume the electron density is known only at the nodes of a uniform grid, whose positions are given by:

$$\boldsymbol{x}_{ijk} = i\boldsymbol{a}_g + j\boldsymbol{b}_g + k\boldsymbol{c}_g \tag{6}$$

where i, j, and k are integers and $\boldsymbol{a}_g$, $\boldsymbol{b}_g$, and $\boldsymbol{c}_g$ are the basis vectors of the grid. The grid is finite and has $\boldsymbol{n} = (n_a, n_b, n_c)$ nodes along each axis so i, j, and k can take values only from 0 to $n_a - 1$, $n_b - 1$, or $n_c - 1$, respectively. If the density corresponds to a periodic solid, the typical case is that the grid spans the unit cell, so the lattice vectors of the crystal ($\boldsymbol{a}_l$, $\boldsymbol{b}_l$, $\boldsymbol{c}_l$) are multiple integers of the grid basis vectors:

$$\boldsymbol{a}_l = n_a\boldsymbol{a}_g \quad ; \quad \boldsymbol{b}_l = n_b\boldsymbol{b}_g \quad ; \quad \boldsymbol{c}_l = n_c\boldsymbol{c}_g \tag{7}$$

In this case, the density is periodic, $\rho(\boldsymbol{x} + \boldsymbol{R}) = \rho(\boldsymbol{x})$, where $\boldsymbol{R}$ is a lattice vector:

$$\boldsymbol{R} = m_a\boldsymbol{a}_l + m_b\boldsymbol{b}_l + m_c\boldsymbol{c}_l \tag{8}$$

with $m_a, m_b, m_c \in \mathbb{Z}$. Consequently, we assume the grid extends periodically and indefinitely in all directions, the integers in Eq. 6 can take any integer value, and the value of the density at grid node $\boldsymbol{x}_{ijk}$ is:

$$\rho_{ijk} = \rho(i \bmod n_a, j \bmod n_b, k \bmod n_c) \tag{9}$$

This makes the grid a lattice in $\mathbb{R}^3$ and the crystal lattice one of its sublattices, with the primitive cell volume of the latter being $n_a n_b n_c$ times the covolume of the former. For the sake of simplicity in the discussion, we will consider that electron density grids for gas-phase molecules are also periodic; critical points found far away from the molecule can be discarded using a density or distance threshold. Lastly, it is important to note that solid-state grids are often non-orthogonal when the crystal lattice is non-orthogonal. In this case, no orthogonal basis for the grid ($\boldsymbol{a}_g, \boldsymbol{b}_g, \boldsymbol{c}_g$) can be chosen.

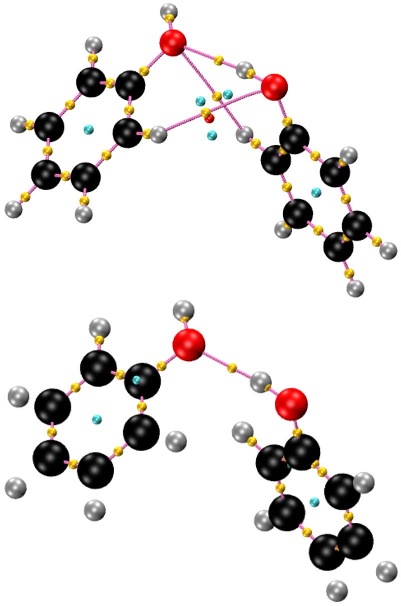

FIG. 1. Critical points and molecular graph for the phenol dimer from the S22 set.[55] Top: calculated using an analytical density. Bottom: using tricubic interpolation on a grid. Bonds, rings, and cages are shown as yellow, cyan, and red small balls, respectively. Bond paths are pink.

The challenges associated with searching CPs of the electron density using interpolation from a uniform grid have been noted in the seminal work of Vega et al.,[39] where three-dimensional Lagrange interpolation was used. While this method works, the authors noted occasional failures in the CP search caused by the derivative discontinuities as the target point moves and the nodes on which the interpolation is based change. Vega et al. also noted the usefulness in interpolating the logarithm of the density, rather than the density itself, to minimize numerical noise, whish is similar to the smoothing transformation presented here (Eq. 20).

To illustrate the difficulties with a CP search using grid interpolation, consider a simple example: the phenol dimer from the S22 set.[55] The wavefunction has been calculated using Gaussian16[56] and the B3LYP/6-31+G$*$ method. The CP search using the default parameters mentioned above yields 26 nuclei, 29 bonds, 5 rings, and one cage, for a correct Poincaré-Hopf sum of 1. Figure 1 (top) shows the distribution of critical points and bond paths in the system. The usual intramolecular bonds were found, as well as the hydrogen bond and a side

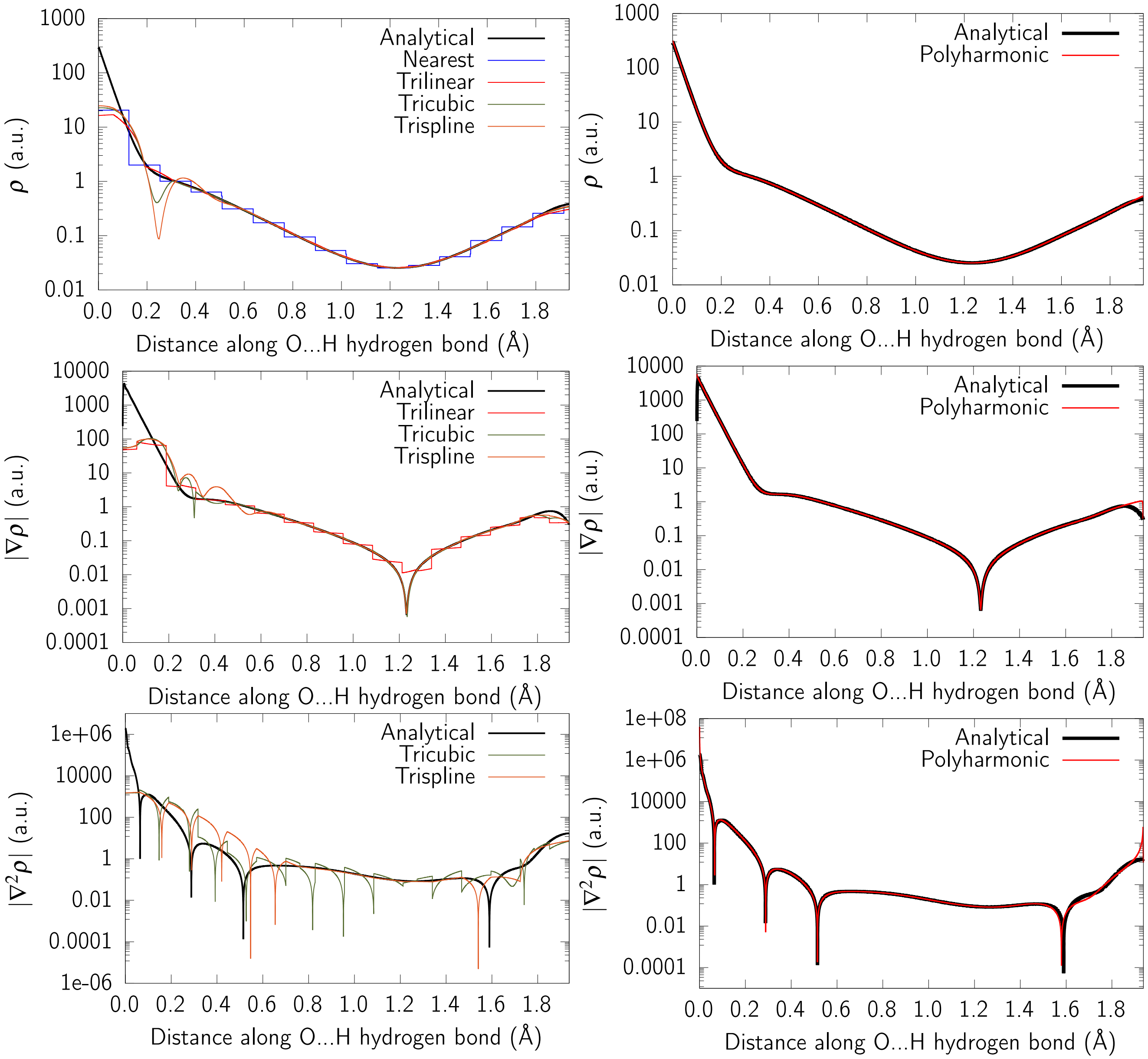

FIG. 2. One-dimensional interpolation along the O. . . H hydrogen bond line in phenol dimer (Fig. 1). Top: electron density, middle: electron density gradient, bottom: absolute value of the Laplacian. Left: using various interpolation functions. Right: using the interpolant proposed in this work.

interaction between the C–H in one phenyl ring and the oxygen of the hydrogen bond acceptor molecule. The phenyl ring critical points as well as the ring and cage critical point structure in the intermolecular region were also correctly found.

Instead of using the analytical density, a grid was generated with 0.125 Å per node in each axis ($n_a = 141$, $n_b = 104$, $n_c = 97$). This is a reasonable value because the analytical density shows that the BCPs along the O-H bond are as close as 0.19 Å to the hydrogen atom, so a coarser grid may not be able to capture these critical points. Using Newton's method (Eq. 5) requires calculating the first and second derivatives at arbitrary points, so three-dimensional interpolation must be used. Four interpolation methods have been tried:

- Nearest: The density at point $\boldsymbol{x}$ in fractional coordinates is taken as the density of grid node $[\boldsymbol{x} \cdot \boldsymbol{n}]$, where $[\cdot]$ denotes the integer rounding function. This interpolant is discontinuous.

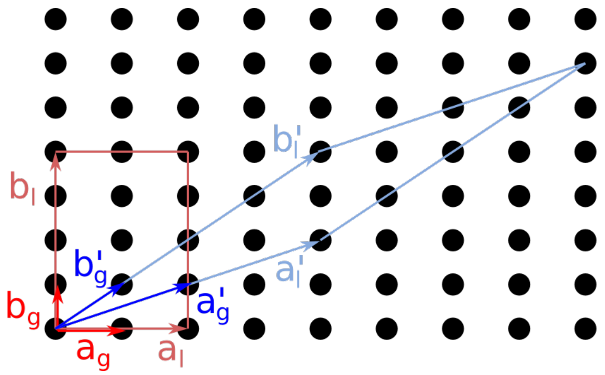

FIG. 3. Two bases are shown for the same grid $\boldsymbol{a}_g$ and $\boldsymbol{b}_g$ in red and $\boldsymbol{a}_g'$ and $\boldsymbol{b}_g'$ in blue. The lattice vectors for the corresponding crystal bases are shown in light blue ($\boldsymbol{a}_l$ and $\boldsymbol{b}_l$) and light red ($\boldsymbol{a}_l'$ and $\boldsymbol{b}_l'$).

- Trilinear:

$$\begin{aligned}\rho(\boldsymbol{x}) = \sum_{ijk=0}^{1} \rho_{n+i,m+j,l+k}\times \\ \times (\delta_{i0}-(-1)^i x)(\delta_{j0}-(-1)^j y)(\delta_{k0}-(-1)^k z)\end{aligned} \tag{10}$$

  where $\boldsymbol{m} = (n,m,l) = \lfloor \boldsymbol{x}\cdot\boldsymbol{n}\rfloor$, $(x,y,z) = \boldsymbol{x}\cdot\boldsymbol{n} - \boldsymbol{m}$, and $\lfloor\cdot\rfloor$ is the floor function. This function is continuous but not differentiable.

- Tricubic:[57]

$$\rho(\boldsymbol{x}) = \sum_{ijk=0}^{3} a_{ijk}x^i y^j z^k \tag{11}$$

  where $\boldsymbol{x} = (x,y,z)$ have the same meaning as in the trilinear interpolation and the 64 a_{ijk} coefficients are determined by 64 constraints involving the value, first derivatives, and mixed second and third derivatives of the density at the eight grid nodes with indices built from combinations of $\lfloor \boldsymbol{x}\cdot\boldsymbol{n}\rfloor$ and $\lceil \boldsymbol{x}\cdot\boldsymbol{n}\rceil$, where $\lceil\cdot\rceil$ is the ceiling function. The derivatives are calculated using finite differences between grid nodes. This interpolant is globally C^1 and has continuous mixed second derivatives.

- Trispline: a tricubic spline interpolation based on the method described in Ref. 58. Cubic splines are determined for every row of nodes in the three grid directions and successive interpolations are carried out on the edges and sides of the parallelepiped encompassing the point of interest $\boldsymbol{x}$. This method has been proposed for the purpose of electron density CP location before,[32] and the actual code in critic2 was adapted from the abinit program.[59,60] This function is continuous up to the second derivatives.

All four interpolation methods predict the density at the grid nodes exactly but vary in their smoothness as the grid nodes from which the density is interpolated, known as the "stencil", change.

Figure 2 (left) shows the density, norm of the density gradient, and absolute value of the Laplacian along the hydrogen bond in phenol dimer for these four interpolation methods compared to the same properties from the analytical density. As shown in the plot, the electron density is reconstructed with relatively good accuracy by all methods (except nearest) in the bond critical point region. However, the performance of all methods degrades both in the regions close to the nuclei and in the calculation of higher-order derivatives. This is true even in the case of the trispline interpolation, which has continuous second derivatives. This problem with the trispline interpolation, which ultimately affects CP location methods, has already been noted by Palatinus et al.,[32] who suggested interpolating derivatives calculated on the grid using finite differences. Katan et al. also suggested using a finer grid.[42]

The result of the CP search using the tricubic interpolation in combination with Newton's method is shown in Figure 1 (bottom). Unsurprisingly given the poor quality of the density derivatives, many CPs are missing, some spurious CPs have appeared, and the Poincaré-Hopf sum rule is violated. While quite a few of the covalent bond paths have been found, some C-H BCPs are missing as well as all the intermolecular rings and cages. Clearly this is not a reliable procedure for general CP location. Although specialized grid-based techniques could be used in place of Newton, ultimately the quality of the interpolation will determine the accuracy of the critical point positions and properties, so it is interesting to try to find a better alternative for the interpolation method. A more accurate interpolant also has the added benefit that no grid-specialized algorithms for the CP search are required, and that it can be used for other purposes that require calculating the electron densities at points outside the grid.

There is a more subtle drawback to the interpolation methods presented above, which underlies the "lattice bias" in Henkelman's grid integration method observed by Tang et al.[36] The same grid can be described with infinitely many bases. This is sketched for a two-dimensional grid in Figure 3. The four methods above use an interpolation stencil whose geometry depends on the choice of grid basis, which is ultimately arbitrary. In addition, accurate interpolation requires the grid nodes on the stencil being close in Euclidean distance to the target point, which may not be the case if the grid basis is bad, i.e. if the basis vectors are long and the angles between them are small. Therefore, values interpolated from the same grid depend on an arbitrary choice of basis and, in the particular case of non-orthogonal grids, some directions in space are privileged relative to others, due to the particular geometry of the interpolation stencil.

This problem affects previously proposed grid-based

QTAIM algorithms, not only those related to CP location. For instance, the EDMA program[32] considers the neighbors of a given grid node to be the 26 adjacent nodes obtained by adding and subtracting the grid basis vectors: $m_a\boldsymbol{a}_g + m_b\boldsymbol{b}_g + m_c\boldsymbol{c}_g$ with $m_i = -1, 0, 1$, and a similar approach is taken by Vega et al.[39] The identity and distance between grid nodes chosen in this way, and therefore the outcome of the method, depend on the arbitrary choice of grid basis. This is also the ultimate reason why Henkelman's integration method had to be revised several times.[34–36] In contrast, the Yu and Trinkle algorithm[37,38] does not have lattice bias by construction because it considers that the neighbors of a given grid node are those given by its Voronoi relevant vectors, which are independent of the grid basis. A grid-based interpolation or CP search algorithm must not give different results depending on the choice of grid basis or show any directional bias. This is particularly relevant in solids because, as mentioned above, solid-state density grids are often non-orthogonal. In the rest of the article, we will use the term "lattice bias" to refer to this problem.

III. POLYHARMONIC SPLINE INTERPOLATION

It is remarkable that, despite the fact that it is continuous up to the second derivatives, the trispline interpolation fails so badly at reproducing the Laplacian of the electron density, which ultimately precludes its use in a Newton-based CP search algorithm.

The method proposed in this work is based on polyharmonic spline interpolation[61–64] combined with a smoothing transformation. Polyharmonic splines combine optimal smoothing properties with flexible stencil selection.[65] A polyharmonic spline interpolant combines radial basis functions with a low-degree polynomial:

$$\rho(\boldsymbol{x}) = \sum_i^N w_i \phi(|\boldsymbol{x} - \boldsymbol{x}_i|) + p(\boldsymbol{x}) \tag{12}$$

where $\{\boldsymbol{x}_i\}$ are the positions of the N grid nodes used in the interpolation stencil. The polynomial term is written as:

$$p(\boldsymbol{x}) = \boldsymbol{v} \cdot (1, \boldsymbol{x})^T \tag{13}$$

The $\boldsymbol{w} = \{w_i\}$ and $\boldsymbol{v} = (v_0, v_x, v_y, v_z)$ are the $N+4$ interpolation coefficients, which are determined by applying the following $N+4$ constraints:

$$\rho(\boldsymbol{x}_i) = f_i \tag{14}$$

$$\sum_i w_i = 0 \tag{15}$$

$$\sum_i w_i \boldsymbol{x}_i = 0 \tag{16}$$

where the sums run over the stencil grid nodes. The application of these constraints leads directly to the following matrix equation:

$$\Phi \left(\boldsymbol{w} \;\; \boldsymbol{v}\right)^T = \begin{pmatrix} F & C \\ C^T & 0 \end{pmatrix} \left(\boldsymbol{w} \;\; \boldsymbol{v}\right)^T = \begin{pmatrix} \boldsymbol{\rho}^T \\ 0 \end{pmatrix} \tag{17}$$

where $\boldsymbol{\rho} = (\rho_1, \ldots, \rho_N)$ is the vector of electron densities at the stencil grid nodes. The symmetric F matrix is defined as:

$$F_{ij} = \phi(|\boldsymbol{x}_i - \boldsymbol{x}_j|) \tag{18}$$

and row i in matrix C is:

$$C_i = (1, \boldsymbol{x}_i) \tag{19}$$

The radial function for a polyharmonic spline of degree 2 in three dimensions, $\phi(r) = r^3$, was used. Polyharmonic splines are commonly used for the interpolation of scattered data.

Figure 1 shows clearly that the main difficulty for the interpolants lies in accurately reconstructing the electron density in the regions close to the nuclei, where $\rho(\boldsymbol{x})$ changes very quickly. In this work, instead of using the electron density directly, the interpolation is carried out on the function resulting from the smoothing transformation:

$$f(\boldsymbol{x}) = \ln\left(\frac{\rho(\boldsymbol{x})}{\rho_0(\boldsymbol{x})}\right) \tag{20}$$

where $\rho_0(\boldsymbol{x})$ is the promolecular density, the sum of atomic in-vacuo densities at the system geometry. (Note there is an arbitrariness[66] in the choice of reference atomic densities for building ρ_0, but we expect any reasonable reference density will do.) In the critic2 implementation, $\rho_0(\boldsymbol{x})$ is known only numerically but, because it is calculated as a sum of contributions from one-dimensional radial functions, its value and its derivatives at an arbitrary point can be calculated very accurately using one-dimensional interpolation. The deformation density $(\rho(\boldsymbol{x}) - \rho_0(\boldsymbol{x}))$, which measures deviations from the promolecular density, is a popular chemical bonding indicator because density accumulates in the interatomic region upon formation of a chemical bond. The function in Eq. 20 also expresses deviations with respect to the promolecular density. Since the changes induced in the electron density by the formation of chemical bonds are relatively minor compared to the density itself and happen mostly in the interatomic regions, where the density varies slowly, $f(\boldsymbol{x})$ is an excellent candidate for a smoothing transformation.

The interpolant built from the polyharmonic spline (Eq. 13) applied to the smooth density function (Eq. 20) has analytical first and second derivatives that can be readily calculated:

$$\tilde{\rho} = \rho_0 \times e^f \tag{21}$$

$$\tilde{\rho}_\xi = \rho \times \left(f_\xi + \frac{\rho_{0\xi}}{\rho_0} \right) \tag{22}$$

$$\tilde{\rho}_{\xi\zeta} = \rho \times \left(f_{\xi\zeta} + \frac{\rho_\xi \rho_\zeta}{\rho^2} + \frac{\rho_{0\xi\zeta}}{\rho_0} - \frac{\rho_{0\xi}\rho_{0\zeta}}{\rho_0^2} \right) \tag{23}$$

where the ξ and ζ subscripts denote the derivatives with respect to the Cartesian coordinates (x, y, z) of the corresponding functions. The derivatives of the smooth function are obtained as the derivatives of the polyharmonic spline:

$$f = \sum_i w_i \phi(r) + \boldsymbol{v} \cdot \boldsymbol{x} + v_0 \tag{24}$$

$$f_\xi = \sum_i w_i \phi'(r) \frac{\boldsymbol{x}_\xi - \boldsymbol{x}_{i\xi}}{r} + \boldsymbol{v}_\xi \tag{25}$$

$$\begin{aligned} f_{\xi\zeta} = \sum_i w_i \Bigg[& \phi''(r) \frac{(\boldsymbol{x}_\xi - \boldsymbol{x}_{i\xi})(\boldsymbol{x}_\zeta - \boldsymbol{x}_{i\zeta})}{r^2} \\ & + \phi'(r) \left(\frac{\delta_{\xi\zeta} r}{r} - \frac{(\boldsymbol{x}_\xi - \boldsymbol{x}_{i\xi})(\boldsymbol{x}_\zeta - \boldsymbol{x}_{i\zeta})}{r^3} \right) \Bigg] \end{aligned} \tag{26}$$

with $\boldsymbol{x}_\xi$ the ξ component of vector $\boldsymbol{x}$, $r = |\boldsymbol{x} - \boldsymbol{x}_i|$, and $\phi'(r) = 3r^2$ and $\phi''(r) = 6r$ are the first and second derivatives of the radial function.

In this work, the number of radial basis functions used is $N = 8^3 = 512$. For a given target point $\boldsymbol{x}$, the N grid nodes on which these functions are based are the closest in Euclidean distance to the nearest grid node $\boldsymbol{x}_0$ (the "base" node). The use of a base node, instead of simply taking the N grid nodes closest to the target point, is important because the stencil geometry and the Φ matrix in Eq. 17 are the same for every target point, which means they can be pre-computed and stored. More importantly, the fact that the stencil nodes are determined by Euclidean distance, rather than by linear combinations of the grid basis vectors, eliminates the lattice bias from the interpolation method since the same grid with two different bases would give the same stencil for a particular target point.

As the target point moves from one base node to another, there is a change in stencil, and therefore the interpolant obtained from simply using $\tilde{\rho}$ (Eq. 21) is not continuous. However, adjacent base nodes share a large part of their stencils. Therefore, in order to address this problem, we build our interpolation function as a linear combination of the interpolants with base nodes in the vicinity of the target point. Specifically, if $\boldsymbol{x}$ is the target point, we assign a weight to each grid node $\boldsymbol{x}_i$ given by:

$$w_i = \begin{cases} \exp\left(\frac{d_i^3}{a^3(d_i^3 - a^3)} \right), & \text{if } 0 \leq d_i < a \\ 0, & \text{if } d_i \geq a \end{cases} \tag{27}$$

where $d_i = |\boldsymbol{x} - \boldsymbol{x_i}|$ and a is a range parameter, which in this work is taken as twice the longest grid step. This weight function has a maximum at $d = 0$ and goes smoothly to zero at $x = a$ with continuous first and second derivatives. The density is then interpolated as:

$$\rho(\boldsymbol{x}) = \frac{\sum_i w_i \tilde{\rho}_i(\boldsymbol{x})}{\sum_i w_i} \tag{28}$$

where $\tilde{\rho}_i(\boldsymbol{x})$ is the density predicted by the interpolant based on node grid i. The first and second derivatives required for the CP location are calculated straightforwardly from Eqs. 27 and 28. This choice of weight function makes the proposed interpolation method have continuous derivatives up to at least second order and devoid of lattice bias.

The dramatic improvement in the accuracy of the interpolation using the new method can be seen in the phenol dimer example, Figure 2 (right). The spurious oscillations in the density and its derivatives have disappeared and the interpolated values are in exceptional agreement with the analytical density, except for minor disagreements very close to the nuclei and in the very steep shell structure of the Laplacian. In the next section, it is shown that the CP topology of a molecule or solid can be recovered when this interpolant is used in combination with Newton's method, yielding accurate properties at the critical points and molecular graphs that are visually indistinguishable from their analytical counterparts.

Regarding the practical details, as mentioned above, the fact that the stencil geometry is independent of the target point position allows an efficient implementation. The Φ matrix, the stencil integer offsets, and the promolecular densities and their derivatives on the grid are precomputed and stored. (In fact, Φ could be saved in decomposed form to speed up the solution of the system of linear equations in Eq. 17.) A single evaluation of the interpolant at an arbitrary target point requires, for every interpolant $\tilde{\rho}_i$ appearing in Eq. 28, the retrieval of the N density values on the grid nodes belonging to the corresponding stencil (right-hand side of Eq. 17), then solving the system to obtain the interpolation coefficients, and finally applying Eqs. 21 to 26 to calculate the interpolated density and its derivatives. The cost of the interpolant evaluation is independent of the grid size and the system size, although the previously mentioned preparatory calculations are not. In addition, CP location based Newton's method is trivially parallelizable, as Newton searches launched from different seeds are independent of each other.

IV. RESULTS

The performance of the proposed method regarding CP location in molecular systems is examined now. This performance is gauged by whether the same critical point topology as the analytical electron density is recovered. That is, there must be no missing or extra critical points.

TABLE I. Accuracy in the calculation of critical points and their properties using the proposed interpolation method compared to the analytical critical points. num: number of critical points of each type (the topology is the same with both methods). $\overline{\Delta x}$: average distance between CP positions using the interpolation and analytical densities in Å. MAE(x): mean absolute error for property x in atomic units. MAPE(x) and MaxAPE(x): mean and maximum absolute percent error for property x in %.

System	CP type	num	$\overline{\Delta x}$		ρ			$\nabla^2\rho$	
				MAE	MAPE	MaxAPE	MAE	MAPE	MaxAPE
Phenol dimer	nucleus	26							
	bond	29	0.000 812	6.416×10^{-5}	0.0204	0.2645	1.580×10^{-2}	1.3153	10.6415
	ring	5	0.000 190	1.040×10^{-6}	0.0061	0.0301	1.243×10^{-4}	0.1186	0.2200
	cage	1	0.000 047	2.650×10^{-9}	0.0001	0.0001	3.473×10^{-6}	0.0233	0.0233
C_{60}	nucleus	60							
	bond	90	0.000 114	1.271×10^{-5}	0.0042	0.0439	4.427×10^{-3}	0.5736	3.7203
	ring	32	0.000 208	4.688×10^{-6}	0.0148	0.0301	4.799×10^{-4}	0.2369	0.7967
	cage	1	0.000 001	9.970×10^{-11}	0.0003	0.0003	4.833×10^{-8}	0.0459	0.0459
S12L 4b complex	nucleus	158							
	bond	225	0.000 422	2.442×10^{-5}	0.0086	0.1655	6.861×10^{-3}	0.7472	9.3189
	ring	78	0.000 301	2.502×10^{-6}	0.0086	0.0284	4.294×10^{-4}	0.2149	0.8154
	cage	10	0.000 094	3.399×10^{-8}	0.0010	0.0019	9.086×10^{-6}	0.0669	0.1121
Water hexamer	nucleus	18							
	bond	21	0.001 672	3.375×10^{-4}	0.1037	0.3348	7.596×10^{-2}	4.0819	12.4118
	ring	5	0.000 123	7.102×10^{-8}	0.0022	0.0044	2.368×10^{-5}	0.0919	0.1697
	cage	1	0.000 081	3.433×10^{-8}	0.0022	0.0022	9.200×10^{-6}	0.1416	0.1416
KB49 set	bond		0.001 097	1.009×10^{-4}	0.0342	0.5998	3.000×10^{-2}	5.6095	259.3543
	ring		0.000 267	5.463×10^{-7}	0.0029	0.0207	1.342×10^{-4}	0.3186	2.0845
	cage		0.000 278	5.342×10^{-8}	0.0013	0.0050	6.388×10^{-5}	0.4393	1.3025

Another important performance measure is the accuracy of the properties calculated at the critical points found, particularly the electron density and Laplacian.

Four molecules and supramolecular complexes with increasing complexity are examined: the phenol dimer from the S22 set[55] used in Section II, a water hexamer in the prism geometry,[67] a C_{60} fullerene,[68,69] and complex 4b (a C_{70} catcher complex) from the S12L set.[70] All calculations were carried out at the geometries reported in the literature using Gaussian16[56] and the B3LYP/6-31+G∗ method. (We do not expect significant changes in performance with the level of theory, see Table 1 in the Supporting Information.) The analytical wavefunction was used to generate orthogonal grids with 0.125 Å per node in each axis. The critical point search was carried out in exactly the same way with the analytical and interpolated densities. Critical points with density lower than 1×10^{-5} atomic units were discarded to prevent the appearance of degenerate critical points far from the molecules.

The resulting CP topologies and molecular graphs are shown in Figure 4, and the accuracy in the calculated CP positions and properties for the density and the Laplacian compared to the same quantities from the analytical density are shown in Table I. The calculation of the CP topology took 1 m (water prism), 1.5 m (phenol dimer), 10.5 m (C_{60}), and 41 m (C_{70} pincer) on a modern desktop PC. Further optimizations and fine-tuning to the code can be implemented to speed up the calculations (for instance, the pre-decomposition of the Φ matrix mentioned in Section III).

The number and type of critical points found using the interpolated densities are the same as with the analytical densities, and the Poincaré-Hopf sum rule holds in both cases. Combined with the lack of spurious features of the interpolated topology and bond paths in Figure 4, this result strongly suggests that the polyharmonic interpolation in combination with Netwon's method was successful in recovering all critical points in these systems.

Table I also shows that the CP positions were recovered from the polyharmonic interpolation with high accuracy, considering the distance between grid nodes along a given axis is as high as 0.125 Å. The average distance between the analytical and interpolated CP positions are in the range of approximately 1×10^{-4} Å to 1×10^{-3} Å, with the bonds in water hexamer showing the highest deviation at 0.0017 Å. For reference, these values are about two orders of magnitude lower than the average deviation in CP positions between common density functional approximations and CCSD.[14]

The accuracy in the prediction of properties at the critical points is also good according to Table I. Densities predicted at the critical points by the interpolation method are at most around 1×10^{-4} atomic units (0.1% error), and more typically in the range of 0.01% to 0.001% errors, depending on system and critical point type. As in the case of the positions, this level of accuracy is about 2 orders of magnitude lower than the typical agreement between density functional approximations and CCSD densities.[14] For the Laplacian, the MAE in the worst case is in the range of 1×10^{-2} atomic units (1 to 6% error), but typically much lower, showing that, same as with the other interpolation method, higher-order derivatives suf-

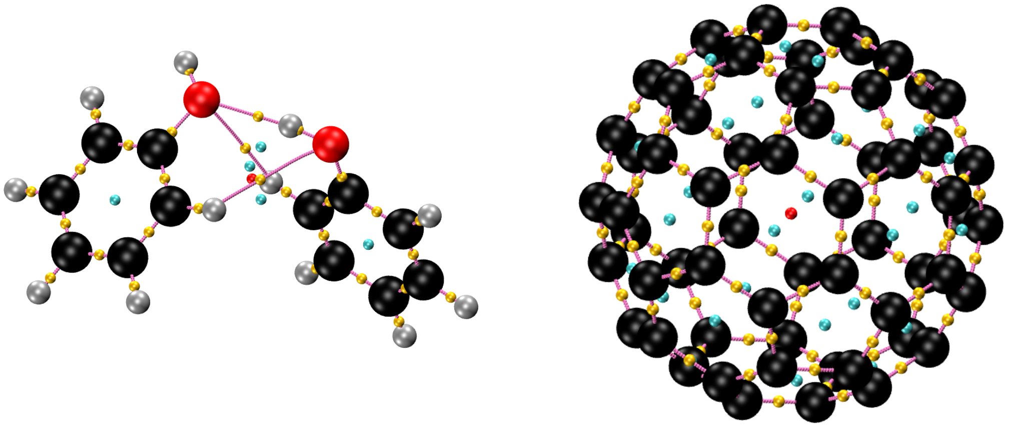

(a) Phenol dimer

(b) C_{60} fullerene

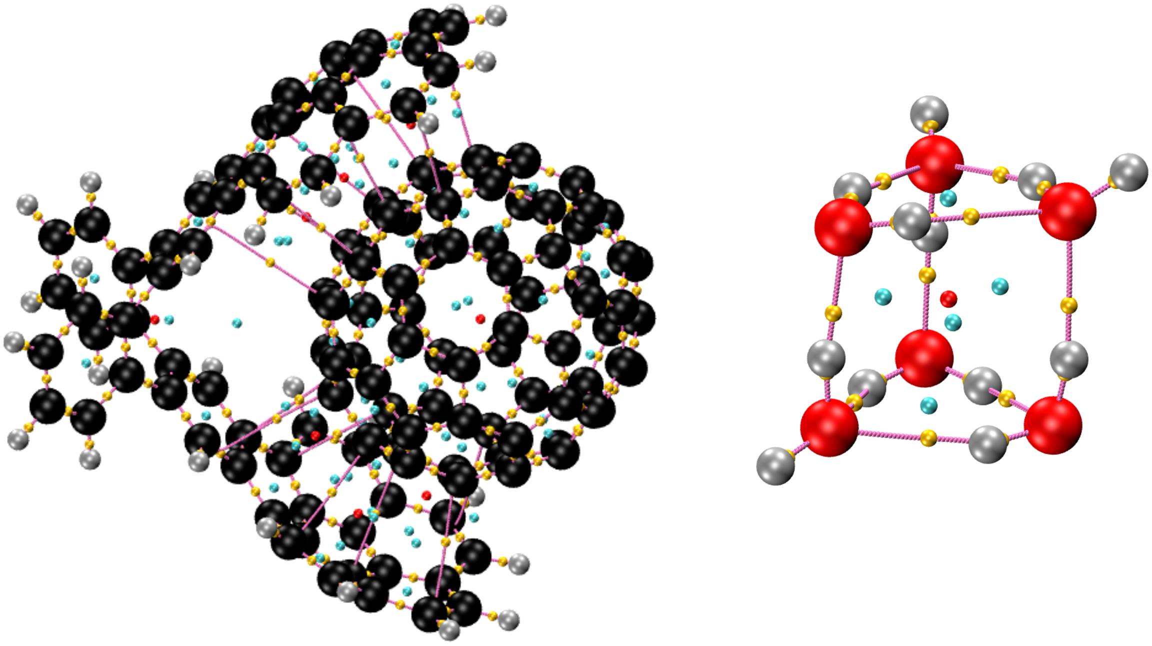

(c) C_{70} pincer complex (4b)

(d) water hexamer (prism)

FIG. 4. Critical point topology and molecular graph of four relatively complex molecules calculated using the proposed interpolation method. Bonds, rings, and cages are shown as yellow, cyan, and red small balls, respectively. Bond paths are pink.

fer a penalty to the accuracy in the interpolation. Still, the average errors for in Table I indicate that the interpolated Laplacian would be perfectly usable for chemical bonding analysis.[1]

The CP topology and the molecular graphs calculated using the interpolation method are shown in Figure 5. The calculation time was less than 2 minutes in all cases on a desktop PC. The number of nuclei, bonds, rings, and cages found, respectively, were: MoS_2 (6, 18, 20, 8), quartz (9, 18, 18, 9), and urea (16, 26, 18, 8). The Morse sum is zero in all cases, and the critical point positions are consistent with the crystal space groups. The number of critical points of each type in the asymmetric unit were: MoS_2 (2, 2, 3, 3), MoS_2 (2, 4, 3, 3), and urea (5, 7, 4, 3). The complete CP topology seems to have been found in the three solids.

In order to verify the robustness of the proposed interpolation method, we calculated the CP topology of all 49 dimers in the Kannemann-Becke set (KB49),[71,72] typically used for fitting the parameters in the exchange-hole dipole dispersion model (XDM).[73] The CP topologies and positions of the critical points calculated by interpolation from the grid agree with the analytical electron density in all 49 systems. Table I also shows the average deviation in the CP position, density, and Laplacian between the interpolated and the analytical densities for the KB49 set. The results are similar to the other hydrogen bonded systems (hydrogen bonds are abundant in the KB49 set), with an average error in the position of about 1×10^{-3} Å for bonds and 3×10^{-4} Å for the other

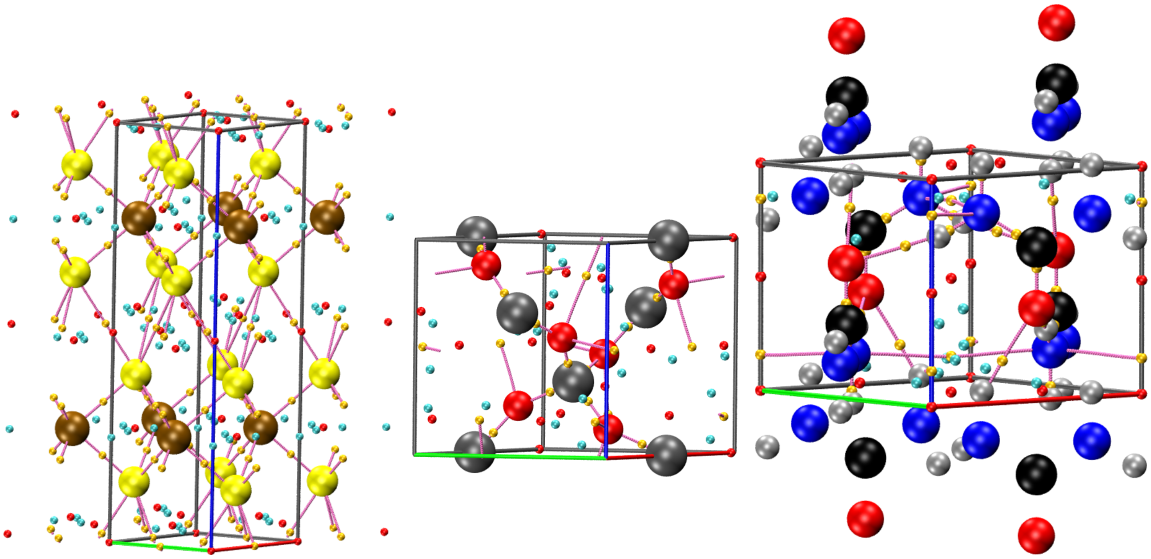
(a) MoS_2 (b) Quartz (c) Urea

FIG. 5. Critical point topology and molecular graph of three periodic solids calculated using the proposed interpolation method. Bonds, rings, and cages are shown as yellow, cyan, and red small balls, respectively. Bond paths are pink.

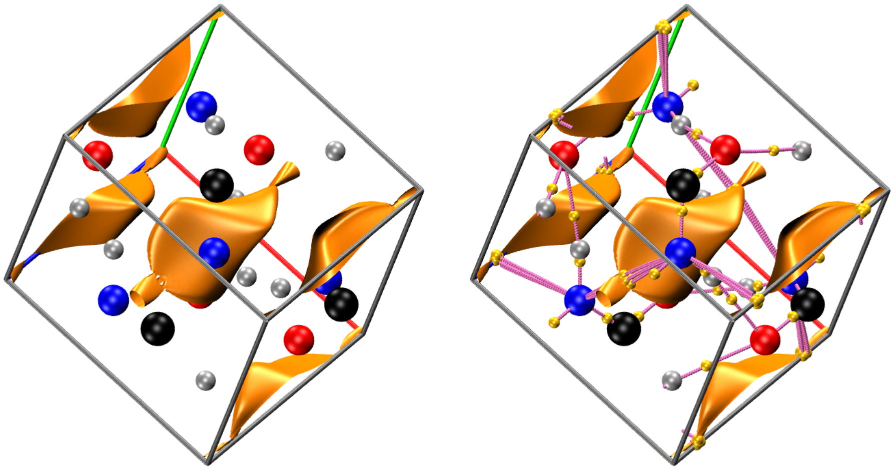

FIG. 6. Left: 0.001175 a.u. density isosurface in urea calculated using Quantum ESPRESSO. Right: the critical point topology and molecular graph are also shown. Bonds, rings, and cages are shown as yellow, cyan, and red small balls, respectively. Bond paths are pink.

CPs. Errors in the density and Laplacian are similarly small, and comparable to the molecules studied above.

Next, the application of the proposed interpolation method is illustrated in a few orthogonal and non-orthogonal periodic solids. The electron densities of urea (space group $P\bar{4}2_1m$), MoS_2 ($P6_3/mmc$), and quartz ($P3_221$) were calculated using the abinit program, version 9.6.2,[59,60] at their experimental geometries. The projector augmented wave (PAW) method[74] was used with datasets from the JTH library.[75] An energy cutoff of 20 Ha was used for the plane waves and 40 Ha was used for the double grid. k-point grids of $4\times4\times4$ (urea and quartz) and $5\times5\times2$ (MoS_2) were employed. The valence density was reconstructed using the PAW transformation, and augmented with the core contributions using critic2's atomic density tables. The grids generated using abinit's default options had approximately 0.09 Å per node in MoS_2 and quartz and 0.17 Å per node in urea.

Lastly, a potential problem that can arise when finding CPs of electron densities in periodic solids from plane wave calculations comes from noise in the low-density regions of the calculated electron densities. For instance, if the PAW calculations for the three crystals above are repeated with Quantum ESPRESSO (QE)[76] using 100 Ry and 1000 Ry cutoffs for the plane-waves and density and datasets from the pslibrary,[77] the correct Morse sum is found in all three crystals, and the CP topology is the same as with abinit for MoS_2 and quartz. However, for urea, even though the Morse sum is zero, extra CPs are found, as shown in Figure 6 (right). The spurious critical points appear on the long N-N intermolecular bond path and they do not disappear if higher cutoffs are used for the density and orbitals. This region has a relatively slowly varying density, so it is possible that the electron density calculated by QE is slightly noisy, possibly as a result of minor aliasing errors. This is suggested by examining the relevant isosurface of the electron density (Figure 6, left), which reveals small oscillations in the region corresponding to this bond critical point. While these ripples in the density are unlikely to affect the energy calculated by QE in any meaningful way, they do generate a number of spurious CPs.

V. APPLICATION TO OTHER SCALAR FIELDS

In this section, we briefly explore the idea of applying the proposed interpolation method to other scalar fields. One particularly relevant scalar field is the molecular electrostatic potential (MESP):

$$V(\boldsymbol{r}) = \sum_A \frac{Z_A}{|\boldsymbol{r} - \boldsymbol{R}_A|} - \int \frac{\rho(\boldsymbol{r}')}{|\boldsymbol{r} - \boldsymbol{r}'|} d\boldsymbol{r}' \tag{29}$$

where A runs over atoms, and $\boldsymbol{R}_A$ are the atomic positions. Extensive work by Gadre and coworkers[22–25,30,78,79] has shown that the MESP contains a wealth of chemical information. The MESP has maxima at the nuclear positions and no non-nuclear maxima.[23] The first-order saddle points mostly coincide with the bond critical points of the density, and the MESP minima indicate regions of local electron density concentration, indicating the presence of lone pairs or electrophilic sites in the molecule.[24] The location of CPs in the MESP (and the density) can be carried out from analytical densities with the DAMQT program of López and coworkers.[25,30,31,80,81]

Here, we are interested in showing that the CPs of the MESP can also be located from a discrete grid of values using the interpolation method proposed above. This is a less efficient method than using analytical expressions[30] but, as in the case of the electron density, this method can be applied to any MESP regardless of source and also in cases where an analytical expression is not available (for instance, if the MESP comes from a plane-wave calculation).

In order to apply our method, a smoothing function different from Eq. 20 has to be chosen, since the MESP can take zero or negative values. The smoothing function used here was:

$$f(\boldsymbol{x}) = \ln\left(\frac{a + V(\boldsymbol{x})}{a + V_0(\boldsymbol{x})}\right) \tag{30}$$

where a is a positive constant value lower than the minimum value taken by the MESP (in this work, $a = 1$ a.u.) and V_0 is the sum of atomic in-vacuo electrostatic potentials. The rest of the method works as described in the previous sections.

As a simple illustration, the interpolation method for MESP grid was applied to four molecules (CO_2, NH_3, H_2CO, and C_2H_4). The calculations were carried out at the same level as in Ref. 31 (M06-L/6-311++G(d,p) for CO_2 and H_2CO, MP2/6-311++G(d,p) for NH_3 and MP2/6-31++G(d,p) for C_2H_4), where the MESP CP topology was found using an approximate analytical expression for the MESP. Same as for previous examples, grids with 0.125 Å per node were generated and the CP search was carried out inside the 0.0001 a.u. density isosurface, in order to remove spurious critical points from the vacuum region.

The resulting topologies are shown in Figure 7 and Table II. The calculated topologies, including the Poincaré-Hopf sum, as well as the CP positions, are the same as those reported using the DAMQT program.[31] The minima of the MESP in these molecules, shown in red in Figure 7 reveals the position of the lone pairs and the center of the π system in acetylene.[24] The value of the MESP at these points is a relevant quantity, which has been shown to correlate with the intermolecular interaction energy in lone pair-π interactions.[79] Table II also shows the values of the MESP at the calculated minima positions obtained by interpolation ($V_{\mathrm{min}}^{\mathrm{interp.}}$) and analytically ($V_{\mathrm{min}}^{\mathrm{anal.}}$). The agreement between the two is excellent, to about 5 significant digits.

While the smoothing function in Eq. 30 is probably not optimal, these results exemplify that the proposed approach can be applied to the analysis of any scalar field whose values are available only on a three-dimensional grid, provided a suitable smoothing function can be found and the grid is fine enough to capture enough details of the underlying scalar function.

VI. CONCLUSIONS

Electron densities and other scalar fields given on a grid are a common occurrence in practical computational chemistry. In this work, two topics are explored: the reconstruction of the electron density from a uniform grid by interpolation and the location of its critical points. The latter is important in the application of the quantum theory of atoms in molecules (QTAIM) to solid-state densities, as the popular plane-wave methods work exclusively with density grids and no analytical representation of the electron density is available.

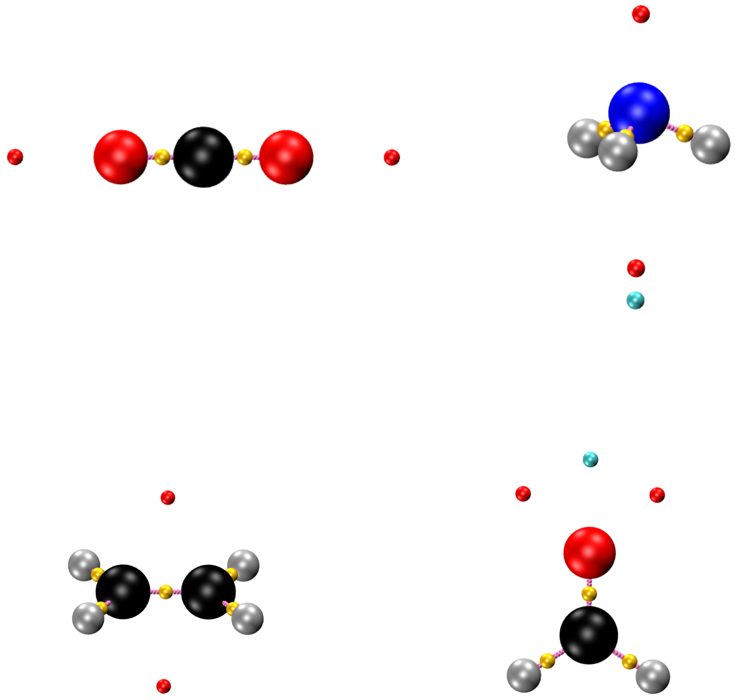

FIG. 7. Critical point topologies of the molecular electrostatic potential in CO_2 (top left), ammonia (top right), ethylene (bottom left), and formaldehyde (bottom right). First-order saddles, second-order saddles, and minima are shown as yellow, cyan, and red small balls, respectively. The gradient paths associated with the first-order saddle points are shown in pink.

TABLE II. Critical point topologies of the molecular electrostatic potential in four molecules calculated using the proposed interpolation method. The number of maxima (n), first-order saddles (b), second-order saddles (r), and minima (c) as well as the Poincaré-Hopf relation (Eq. 4) are shown. The last two columns show the value of the MESP at the minima calculated by interpolation ($V_{\mathrm{min}}^{\mathrm{interp.}}$) and analytically ($V_{\mathrm{min}}^{\mathrm{anal.}}$).

	n	b	r	c	PH	$V_{\mathrm{min}}^{\mathrm{interp.}}$	$V_{\mathrm{min}}^{\mathrm{anal.}}$
CO_2	3	2	0	2	-1	$-2.268\,49 \times 10^{-2}$	$-2.268\,66 \times 10^{-2}$
NH_3	4	3	1	2	0	$1.066\,71 \times 10^{-2}$	$1.066\,72 \times 10^{-2}$
						$-1.236\,28 \times 10^{-1}$	$-1.236\,20 \times 10^{-1}$
C_2H_4	6	5	0	2	-1	$-3.512\,84 \times 10^{-2}$	$-3.512\,82 \times 10^{-2}$
H_2CO	4	3	1	2	0	$-6.282\,57 \times 10^{-2}$	$-6.282\,61 \times 10^{-2}$

In this work, it was shown that the naive application of common interpolation methods to an electron density grid fails to accurately reproduce its features in the steep regions close to the nuclei and also in the calculation of higher-order derivatives. In addition, these interpolation methods are affected by lattice bias, the fact that the outcome of the interpolation depends on the arbitrary choice of basis for the grid. Lattice bias is an important problem because solid-state grids are often non-orthogonal, and this grid basis dependence introduces preferential directions in the system. Lattice bias affects previously proposed grid-based QTAIM algorithms, most notably atomic basin integration methods.

A new reconstruction method for the electron density is proposed based on three-dimensional polyharmonic spline interpolation combined with a smoothing transformation using the promolecular density. The new method has been shown to accurately reproduce the analytical electron density and its derivatives and is not affected by lattice bias. The new interpolant can be used whenever the electron density is required outside the grid, for instance, when plotting or carrying out density-based chemical bonding analysis studies.

The proposed interpolant was then used to perform critical point searches in various molecular and solid-state systems in combination with Newton's method, which requires accurate first and second derivatives to give meaningful results. It was shown that, for most systems, the complete CP topology of the system was recovered and that the CP positions and their density and Laplacian matched their analytical counterparts with high accuracy. In addition, the new CP search method is trivially parallelizable and, because the polyharmonic interpolant is not affected by lattice bias, can be applied to non-orthogonal crystals without introducing spurious directional bias. One potential source of problems identified in solid-state CP topology calculations is noise from the electronic structure method, possibly originating from aliasing error. In summary, this work is a step forward in the development of a CP search method for scalar fields on a grid that is robust, automatic, and accurate.

VII. SUPPLEMENTAL MATERIAL

Table containing the critical point topology and properties for water dimer using B3LYP/6-31+G∗ and CCSD/aug-cc-pVTZ.

VIII. ACKNOWLEDGEMENTS

Financial support from the Spanish Ministerio de Ciencia e Innovación and the Agencia Estatal de Investigación (AEI) (project PGC2018-097520-A-100), the Principality of Asturias (FICYT) and FEDER (project AYUD/2021/51036), and the Spanish MINECO (RyC-2016-20301) are gratefully acknowledged.

IX. DATA AVAILABILITY

The data that support the findings of this study are available from the corresponding author upon reasonable request.

REFERENCES

[1] R. F. W. Bader and H. Essén, "The characterization of atomic interactions," J. Chem. Phys. **80**, 1943–1960 (1984).

[2] R. F. W. Bader, "Atoms in molecules," Acc. Chem. Res. **18**, 9–15 (1985).

[3] R. F. W. Bader, *Atoms in Molecules. A Quantum Theory* (Oxford University Press, Oxford, 1990).

[4] R. F. W. Bader, "A quantum-theory of molecular-structure and its applications," Chem. Rev. **91**, 893–928 (1991).

[5] R. Boyd and C. Matta, *The Quantum Theory of Atoms in Molecules: From Solid State to DNA and Drug Design* (Wiley-VCH, Weinheim, Germany, 2007).

[6] E. Espinosa, M. Souhassou, H. Lachekar, and C. Lecomte, "Topological analysis of the electron density in hydrogen bonds," Acta Cryst. B **55**, 563–572 (1999).

[7] C. Gatti, "Chemical bonding in crystals: new directions," Z. Kristallogr.-Cryst. Mater. **220**, 399–457 (2005).

[8] C. Gatti and P. Macchi, "A guided tour through modern charge density analysis," in *Modern Charge-Density Analysis*, edited by C. Gatti and P. Macchi (Springer Netherlands, Dordrecht, 2012) pp. 1–78.

[9] U. Koch and P. L. A. Popelier, "Characterization of CHO hydrogen bonds on the basis of the charge density," J. Phys. Chem. **99**, 9747–9754 (1995).

[10] E. Espinosa, I. Alkorta, J. Elguero, and E. Molins, "From weak to strong interactions: A comprehensive analysis of the topological and energetic properties of the electron density distribution involving X–H...F–Y systems," J. Chem. Phys. **117**, 5529–5542 (2002).

[11] S. Emamian, T. Lu, H. Kruse, and H. Emamian, "Exploring nature and predicting strength of hydrogen bonds: A correlation analysis between atoms-in-molecules descriptors, binding energies, and energy components of symmetry-adapted perturbation theory," J. Comput. Chem. **40**, 2868–2881 (2019).

[12] S. J. Grabowski, "QTAIM characteristics of halogen bond and related interactions," J. Phys. Chem. A **116**, 1838–1845 (2012).

[13] A. Shahi and E. Arunan, "Hydrogen bonding, halogen bonding and lithium bonding: an atoms in molecules and natural bond orbital perspective towards conservation of total bond order, inter-and intra-molecular bonding," Phys. Chem. Chem. Phys. **16**, 22935–22952 (2014).

[14] E. Brémond, V. Tognetti, H. Chermette, J. C. Sancho-García, L. Joubert, and C. Adamo, "Electronic energy and local property errors at QTAIM critical points while climbing Perdew's ladder of density-functional approximations," J. Chem. Theory Comput. **18**, 293–308 (2022).

[15] R. F. W. Bader, "A bond path: a universal indicator of bonded interactions," J. Phys. Chem. A **102**, 7314–7323 (1998).

[16] A. Martín-Pendás, E. Francisco, M. A. Blanco, and C. Gatti, "Bond paths as privileged exchange channels," Chem. Eur. J. **13**, 9362–9371 (2007).

[17] R. F. W. Bader, "Bond paths are not chemical bonds," J. Phys. Chem. A **113**, 10391–10396 (2009).

[18] P. L. A. Popelier, "On the full topology of the laplacian of the electron density," Coord. Chem. Rev. **197**, 169–189 (2000).

[19] A. Otero-de-la-Roza and V. Luaña, "Topological characterization of the electron density laplacian in crystals. the case of the group IV elements," J. Chem. Theory Comput. (2011).

[20] A. D. Becke and K. E. Edgecombe, "A simple measure of electron localization in atomic and molecular systems," J. Chem. Phys. **92**, 5397 (1990).

[21] B. Silvi and A. Savin, "Classification of chemical bonds based on topological analysis of electron localization functions," Nature **371**, 683–686 (1994).

[22] S. R. Gadre, S. A. Kulkarni, and I. H. Shrivastava, "Molecular electrostatic potentials: A topographical study," J. Chem. Phys. **96**, 5253–5260 (1992).

[23] R. K. Pathak and S. R. Gadre, "Maximal and minimal characteristics of molecular electrostatic potentials," J. Chem. Phys. **93**, 1770–1773 (1990).

[24] A. Kumar, S. R. Gadre, N. Mohan, and C. H. Suresh, "Lone pairs: an electrostatic viewpoint," J. Phys.

Chem. A **118**, 526–532 (2014).

[25]R. López, J. F. Rico, G. Ramírez, I. Ema, D. Zorrilla, A. Kumar, S. D. Yeole, and S. R. Gadre, "Topology of molecular electron density and electrostatic potential with damqt," Comput. Phys. Commun. **214**, 207–215 (2017).

[26]P. L. A. Popelier, "Quantum chemical topology: on bonds and potentials," in *Intermolecular Forces and Clusters I* (Springer, 2005) pp. 1–56.

[27]P. L. A. Popelier and É. A. G. Brémond, "Geometrically faithful homeomorphisms between the electron density and the bare nuclear potential," Int. J. Quantum Chem. **109**, 2542–2553 (2009).

[28]P. L. A. Popelier, "A robust algorithm to locate automatically all types of critical points in the charge density and its laplacian," Chem. Phys. Lett. **228**, 160–164 (1994).

[29]N. O. J. Malcolm and P. L. A. Popelier, "An improved algorithm to locate critical points in a 3D scalar field as implemented in the program MORPHY," J. Comput. Chem. **24**, 437–442 (2003).

[30]S. D. Yeole, R. López, and S. R. Gadre, "Rapid topography mapping of scalar fields: Large molecular clusters," J. Chem. Phys. **137**, 074116 (2012).

[31]A. Kumar, S. D. Yeole, S. R. Gadre, R. López, J. F. Rico, G. Ramírez, I. Ema, and D. Zorrilla, "DAMQT 2.1.0: A new version of the damqt package enabled with the topographical analysis of electron density and electrostatic potential in molecules," J. Comput. Chem. **36**, 2350–2359 (2015).

[32]L. Palatinus, S. J. Prathapa, and S. v. Smaalen, "EDMA: a computer program for topological analysis of discrete electron densities," J. Appl. Cryst. **45**, 575–580 (2012).

[33]M. Kohout, "Dgrid, version 5.2," (Dresden, 2021).

[34]G. Henkelman, A. Arnaldsson, and H. Jonsson, "A fast and robust algorithm for Bader decomposition of charge density," Comput. Mater. Sci. **36**, 354–360 (2006).

[35]E. Sanville, S. D. Kenny, R. Smith, and G. Henkelman, "Improved grid-based algorithm for Bader charge allocation," J. Comput. Chem. **28**, 899–908 (2007).

[36]W. Tang, E. Sanville, and G. Henkelman, "A grid-based Bader analysis algorithm without lattice bias," J. Phys. Condens. Matter **21**, 084204 (2009).

[37]M. Yu and D. R. Trinkle, "Accurate and efficient algorithm for Bader charge integration," J. Chem. Phys. **134**, 064111 (2011).

[38]M. Yu, D. R. Trinkle, and R. M. Martin, "Energy density in density functional theory: Application to crystalline defects and surfaces," Phys. Rev. B **83**, 115113 (2011).

[39]D. Vega, Y. Aray, and J. Rodríguez, "C library for topological study of the electronic charge density," J. Comput. Chem. **33**, 2526–2531 (2012).

[40]H. Bhatia, A. G. Gyulassy, V. Lordi, J. E. Pask, V. Pascucci, and P.-T. Bremer, "TopoMS: Comprehensive topological exploration for molecular and condensed-matter systems," J. Comput. Chem. **39**, 936–952 (2018).

[41]M. Souhassou and R. H. Blessing, "Topological analysis of experimental electron densities," J. Appl. Cryst. **32**, 210–217 (1999).

[42]C. Katan, P. Rabiller, C. Lecomte, M. Guezo, V. Oison, and M. Souhassou, "Numerical computation of critical properties and atomic basins from three-dimensional grid electron densities," J. Appl. Cryst. **36**, 65–73 (2003).

[43]A. Otero-de-la-Roza, M. A. Blanco, A. Martín Pendás, and V. Luaña, "Critic: a new program for the topological analysis of solid-state electron densities," Comput. Phys. Commun. **180**, 157–166 (2009).

[44]A. Otero-de-la-Roza, E. R. Johnson, and V. Luaña, "Critic2: a program for real-space analysis of quantum chemical interactions in solids," Comput. Phys. Commun. **185**, 1007–1018 (2014).

[45]R. Forman, "A user's guide to discrete morse theory." Sémin. Lothar. Comb. **48**, B48c–35 (2002).

[46]A. Gyulassy, P.-T. Bremer, B. Hamann, and V. Pascucci, "A practical approach to Morse-Smale complex computation: Scalability and generality," IEEE Trans. Vis. Comput. Graph. **14**, 1619–1626 (2008).

[47]A. Gyulassy, N. Kotava, M. Kim, C. D. Hansen, H. Hagen, and V. Pascucci, "Direct feature visualization using Morse-Smale complexes," IEEE Trans. Vis. Comput. Graph. **18**, 1549–1562 (2011).

[48]A. Gyulassy, P.-T. Bremer, and V. Pascucci, "Computing Morse-Smale complexes with accurate geometry," IEEE Trans. Vis. Comput. Graph. **18**, 2014–2022 (2012).

[49]A. Gyulassy, D. Günther, J. A. Levine, J. Tierny, and V. Pascucci, "Conforming Morse-Smale complexes," IEEE Trans. Vis. Comput. Graph. **20**, 2595–2603 (2014).

[50]A. Gyulassy, P.-T. Bremer, and V. Pascucci, "Shared-memory parallel computation of morse-smale complexes with improved accuracy," IEEE Trans. Vis. Comput. Graph. **25**, 1183–1192 (2018).

[51]H. Bhatia *et al.*, "Topoms, version 1.1," `https://github.com/LLNL/TopoMS` (2018).

[52]B. B. Iversen, F. K. Larsen, M. Souhassou, and M. Takata, "Experimental evidence for the existence of non-nuclear maxima in the electron-density distribution of metallic beryllium. A comparative study of the maximum entropy method and the multipole refinement method," Acta Cryst. B **51**, 580–591 (1995).

[53]G. K. H. Madsen, P. Blaha, and K. Schwarz, "On the existence of non-nuclear maxima in simple metals," J. Chem. Phys. **117**, 8030–8035 (2002).

[54]V. Luana, P. Mori-Sánchez, A. Costales, M. A. Blanco, and A. Martín-Pendás, "Non-nuclear maxima of the electron density on alkaline metals," J. Chem. Phys. **119**, 6341–6350 (2003).

[55]P. Jurečka, J. Šponer, J. Černỳ, and P. Hobza, "Benchmark database of accurate (MP2 and CCSD(T) complete basis set limit) interaction energies of small model

complexes, DNA base pairs, and amino acid pairs," Phys. Chem. Chem. Phys. **8**, 1985–1993 (2006).

[56] M. J. Frisch, G. W. Trucks, H. B. Schlegel, G. E. Scuseria, M. A. Robb, J. R. Cheeseman, G. Scalmani, V. Barone, G. A. Petersson, H. Nakatsuji, X. Li, M. Caricato, A. V. Marenich, J. Bloino, B. G. Janesko, R. Gomperts, B. Mennucci, H. P. Hratchian, J. V. Ortiz, A. F. Izmaylov, J. L. Sonnenberg, D. Williams-Young, F. Ding, F. Lipparini, F. Egidi, J. Goings, B. Peng, A. Petrone, T. Henderson, D. Ranasinghe, V. G. Zakrzewski, J. Gao, N. Rega, G. Zheng, W. Liang, M. Hada, M. Ehara, K. Toyota, R. Fukuda, J. Hasegawa, M. Ishida, T. Nakajima, Y. Honda, O. Kitao, H. Nakai, T. Vreven, K. Throssell, J. A. Montgomery, Jr., J. E. Peralta, F. Ogliaro, M. J. Bearpark, J. J. Heyd, E. N. Brothers, K. N. Kudin, V. N. Staroverov, T. A. Keith, R. Kobayashi, J. Normand, K. Raghavachari, A. P. Rendell, J. C. Burant, S. S. Iyengar, J. Tomasi, M. Cossi, J. M. Millam, M. Klene, C. Adamo, R. Cammi, J. W. Ochterski, R. L. Martin, K. Morokuma, O. Farkas, J. B. Foresman, and D. J. Fox, "Gaussian 16 Revision A.03," (2016), Gaussian Inc. Wallingford CT.

[57] F. Lekien and J. Marsden, "Tricubic interpolation in three dimensions," Int. J. Numer. Methods Eng. **63**, 455–471 (2005).

[58] W. H. Press, B. P. Flannery, S. A. Teukolsky, and W. T. Vetterling, *Numerical recipes – The art of scientific computing* (Cambridge U. P., Cambridge, 1986).

[59] X. Gonze, B. Amadon, G. Antonius, F. Arnardi, L. Baguet, J.-M. Beuken, J. Bieder, F. Bottin, J. Bouchet, E. Bousquet, N. Brouwer, F. Bruneval, G. Brunin, T. Cavignac, J.-B. Charraud, W. Chen, M. Côté, S. Cottenier, J. Denier, G. Geneste, P. Ghosez, M. Giantomassi, Y. Gillet, O. Gingras, D. R. Hamann, G. Hautier, X. He, N. Helbig, N. Holzwarth, Y. Jia, F. Jollet, W. Lafargue-Dit-Hauret, K. Lejaeghere, M. A. L. Marques, A. Martin, C. Martins, H. P. C. Miranda, F. Naccarato, K. Persson, G. Petretto, V. Planes, Y. Pouillon, S. Prokhorenko, F. Ricci, G.-M. Rignanese, A. H. Romero, M. M. Schmitt, M. Torrent, M. J. van Setten, B. V. Troeye, M. J. Verstraete, G. Zérah, and J. W. Zwanziger, "The Abinit project: Impact, environment and recent developments," Comput. Phys. Commun. **248**, 107042 (2020).

[60] A. H. Romero, D. C. Allan, B. Amadon, G. Antonius, T. Applencourt, L. Baguet, J. Bieder, F. Bottin, J. Bouchet, E. Bousquet, F. Bruneval, G. Brunin, D. Caliste, M. Côté, J. Denier, C. Dreyer, P. Ghosez, M. Giantomassi, Y. Gillet, O. Gingras, D. R. Hamann, G. Hautier, F. Jollet, G. Jomard, A. Martin, H. P. C. Miranda, F. Naccarato, G. Petretto, N. A. Pike, V. Planes, S. Prokhorenko, T. Rangel, F. Ricci, G.-M. Rignanese, M. Royo, M. Stengel, M. Torrent, M. J. van Setten, B. V. Troeye, M. J. Verstraete, J. Wiktor, J. W. Zwanziger, and X. Gonze, "ABINIT: Overview, and focus on selected capabilities," J. Chem. Phys. **152**, 124102 (2020).

[61] J. Duchon, "Splines minimizing rotation-invariant semi-norms in Sobolev spaces," in *Constructive theory of functions of several variables* (Springer, 1977) pp. 85–100.

[62] N. Dyn, "Interpolation of scattered data by radial functions," in *Topics in multivariate approximation* (Elsevier, 1987) pp. 47–61.

[63] M. D. Buhmann, "Radial basis functions," Acta Numer. **9**, 1–38 (2000).

[64] A. Iske, "On the approximation order and numerical stability of local Lagrange interpolation by polyharmonic splines," in *Modern developments in multivariate approximation* (Springer, 2003) pp. 153–165.

[65] A. Iske, "Ten good reasons for using polyharmonic spline reconstruction in particle fluid flow simulations," in *Continuum Mechanics, Applied Mathematics and Scientific Computing: Godunov's Legacy* (Springer, 2020) pp. 193–199.

[66] F. Heidar-Zadeh, P. W. Ayers, T. Verstraelen, I. Vinogradov, E. Vöhringer-Martínez, and P. Bultinck, "Information-theoretic approaches to atoms-in-molecules: Hirshfeld family of partitioning schemes," J. Phys. Chem. A **122**, 4219–4245 (2017).

[67] B. Temelso, K. A. Archer, and G. C. Shields, "Benchmark structures and binding energies of small water clusters with anharmonicity corrections," J. Phys. Chem. A **115**, 12034–12046 (2011).

[68] R. Sure, A. Hansen, P. Schwerdtfeger, and S. Grimme, "Comprehensive theoretical study of all 1812 C_{60} isomers," Phys. Chem. Chem. Phys. **19**, 14296–14305 (2017).

[69] L. Goerigk, A. Hansen, C. Bauer, S. Ehrlich, A. Najibi, and S. Grimme, "A look at the density functional theory zoo with the advanced GMTKN55 database for general main group thermochemistry, kinetics and noncovalent interactions," Phys. Chem. Chem. Phys. **19**, 32184–32215 (2017).

[70] T. Risthaus and S. Grimme, "Benchmarking of London dispersion-accounting density functional theory methods on very large molecular complexes," J. Chem. Theory Comput. **9**, 1580–1591 (2013).

[71] F. O. Kannemann and A. D. Becke, "Van der waals interactions in density-functional theory: Rare-gas diatomics," J. Chem. Theory Comput. **5**, 719–727 (2009).

[72] F. O. Kannemann and A. D. Becke, "van der waals interactions in density-functional theory: Intermolecular complexes," J. Chem. Theory Comput. **6**, 1081–1088 (2010).

[73] A. Otero-de-la-Roza and E. R. Johnson, "Non-covalent interactions and thermochemistry using xdm-corrected hybrid and range-separated hybrid density functionals," J. Chem. Phys. **138**, 204109 (2013).

[74] P. E. Blöchl, "Projector augmented-wave method," Phys. Rev. B **50**, 17953 (1994).

[75] F. Jollet, M. Torrent, and N. Holzwarth, "Generation of projector augmented-wave atomic data: A 71 element validated table in the XML format," Comput. Phys.

Commun. **185**, 1246–1254 (2014).

[76] P. Giannozzi, O. Andreussi, T. Brumme, O. Bunau, M. B. Nardelli, M. Calandra, R. Car, C. Cavazzoni, D. Ceresoli, M. Cococcioni, *et al.*, "Advanced capabilities for materials modelling with quantum espresso," J. Phys.: Condens. Matter **29**, 465901 (2017).

[77] A. Dal Corso, "Pseudopotentials periodic table: From h to pu," Comput. Mater. Sci. **95**, 337–350 (2014).

[78] M. M. Deshmukh, S. R. Gadre, R. Tonner, and G. Frenking, "Molecular electrostatic potentials of divalent carbon (0) compounds," Phys. Chem. Chem. Phys. **10**, 2298–2301 (2008).

[79] N. Mohan, C. H. Suresh, A. Kumar, and S. R. Gadre, "Molecular electrostatics for probing lone pair–π interactions," Phys. Chem. Chem. Phys. **15**, 18401–18409 (2013).

[80] R. López, J. F. Rico, G. Ramírez, I. Ema, and D. Zorrilla, "DAMQT: A package for the analysis of electron density in molecules," Comput. Phys. Commun. **180**, 1654–1660 (2009).

[81] R. López, J. F. Rico, G. Ramírez, I. Ema, and D. Zorrilla, "DAMQT 2.0: A new version of the DAMQT package for the analysis of electron density in molecules," Comput. Phys. Commun. **192**, 289–294 (2015).